The Astrophysical Journal, 681:1148–1162, 2008 July 10

GALACTIC SPIRAL SHOCKS WITH THERMAL INSTABILITY

Chang-Goo Kim,[1] Woong-Tae Kim,[1] and Eve C. Ostriker[2]

Received 2008 February 17; accepted 2008 April 1

ABSTRACT

Using one-dimensional hydrodynamic simulations including interstellar heating, cooling, and thermal conduction, we investigate nonlinear evolution of gas flow across galactic spiral arms. We model the gas as a non-self-gravitating, unmagnetized fluid and follow its interaction with a stellar spiral potential in a local frame comoving with the stellar pattern. Initially uniform gas with density n_0 in the range $0.5\ \mathrm{cm}^{-3} \leq n_0 \leq 10\ \mathrm{cm}^{-3}$ rapidly separates into warm and cold phases as a result of thermal instability (TI) and also forms a quasi-steady shock that prompts phase transitions. After saturation, the flow follows a recurring cycle: warm and cold phases in the interarm region are shocked and immediately cool to become a denser cold medium in the arm; postshock expansion reduces the mean density to the unstable regime in the transition zone and TI subsequently mediates evolution back into warm and cold interarm phases. For our standard model with $n_0 = 2\ \mathrm{cm}^{-3}$, the gas resides in the dense arm, thermally unstable transition zone, and interarm region for 14%, 22%, and 64% of the arm-to-arm crossing time, respectively. These regions occupy 1%, 16%, and 83% of the arm-to-arm distance, respectively. Gas at intermediate temperatures (i.e., neither warm stable nor cold states) represents ~25%–30% of the total mass, similar to the fractions estimated from H I observations (larger interarm distances could reduce this mass fraction, whereas other physical processes associated with star formation could increase it). Despite transient features and multiphase structure, the time-averaged shock profiles can be matched to that of a diffusive isothermal medium with temperature 1000 K (which is $\ll T_{\mathrm{warm}}$) and a "particle" mean free path of $l_0 = 100$ pc. Finally, we quantify numerical conductivity associated with translational motion of phase-separated gas on the grid and show that convergence of numerical results requires the numerical conductivity to be comparable to or smaller than the physical conductivity.

Subject headings: galaxies: ISM — instabilities — ISM: kinematics and dynamics — methods: numerical — stars: formation

1. INTRODUCTION

Spiral arms are the most prominent features in disk galaxies. As the interstellar medium (ISM) passes through the moderate gravitational potential well of the stellar spiral arms, it is strongly compressed and shocked, producing narrow dust lanes in optical images. Active star formation is subsequently triggered in high-density clouds inside the arms, resulting in downstream optical arms that contain OB associations and giant H II regions distributed in a "beads on a string" fashion (e.g., Baade 1963; Elmegreen & Elmegreen 1983; Elmegreen et al. 2006; Shetty et al. 2007). Other arm substructures include filamentary gaseous spurs (or feathers) seen in optical extinction, IR emission from dust, and Hα emission from star formation (e.g., Elmegreen 1980; Scoville & Rector 2001; Scoville et al. 2001; Kennicutt 2004; Willner et al. 2004; La Vigne et al. 2006; Gordon 2007) and giant molecular associations and atomic superclouds seen in CO and H I radio observations (e.g., Elmegreen & Elmegreen 1983; Vogel et al. 1988; Rand & Kulkarni 1990; Knapen et al. 1993). The locations of these arm substructures downstream from the primary dust lanes indicate that the shock compression represents the first step in an evolutionary sequence that begins with diffuse ISM gas and ends with star formation (for strongly bound cores) and dispersal (for more weakly self-gravitating structures), although it is uncertain whether spiral arms actually enhance the star formation rate or just organize it (e.g., Gerola & Seiden 1978; Elmegreen & Elmegreen 1986; Sleath & Alexander 1996; Seigar & James 2002).

Studies of galactic spiral shocks date back to Roberts (1969), who used a semianalytic approach to obtain one-dimensional, stationary shock profiles as functions of the distance perpendicular to the shocks (see also Fujimoto 1968; Roberts & Yuan 1970; Shu et al. 1973). Woodward (1975) used time-dependent calculations to show that spiral shocks in local models indeed develop within one or two crossings of the background arm potential. This and subsequent work (e.g., Kim & Ostriker 2002) suggests spiral arm shocks in the one-dimensional approximation are highly stable for a range of the arm strength. On the other hand, spiral shocks have been shown to be intrinsically unstable when the vertical dimension is included (Martos & Cox 1998; Gómez & Cox 2002, 2004; Boley & Durisen 2006; Kim & Ostriker 2006). Since the arm-to-arm crossing periods are in general incommensurable with the vertical oscillation periods, the gas streamlines are not closed, giving rise to shock flapping motions that dump a significant amount of random kinetic energy in the gas (Kim et al. 2006). Under certain (strong compression) conditions, two-dimensional *in-plane* spiral shocks can also become unstable due to strong shear within the arm (Wada & Koda 2004; Dobbs & Bonnell 2006). However, these in-plane modes are stabilized by moderate magnetic fields (Shetty & Ostriker 2006; Dobbs & Price 2008) and suppressed in fully three-dimensional models due to vertical dynamics (Kim & Ostriker 2006).

Inclusion of gaseous self-gravity tends to enhance the arm response and symmetrize the density profile (Lubow et al. 1986) and causes the shock front to move downstream relative to the minimum in the potential (Kim & Ostriker 2002). High postshock density enhances the growth of self-gravitating perturbations within spiral arms, although postshock flow expansion can limit this growth (Balbus & Cowie 1985; Balbus 1988). Using

---

[1] Department of Physics and Astronomy, FPRD, Seoul National University, Seoul 151-742, Korea; kimcg@astro.snu.ac.kr, wkim@astro.snu.ac.kr.

[2] Department of Astronomy, University of Maryland, College Park, MD 20742; ostriker@astro.umd.edu.

two-dimensional simulations with both self-gravity and magnetic fields, Kim & Ostriker (2002) demonstrated that magneto-Jeans instability (in which magnetic tension forces counterbalance the stabilizing Coriolis forces) leads to the formation of both arm spurs and giant molecular associations/giant molecular clouds with realistic properties (see also Lynden-Bell 1966; Elmegreen 1994). Subsequent studies including three-dimensional effects (Kim & Ostriker 2006) and global spiral structure (Shetty & Ostriker 2006) have confirmed these findings.

While recent work has improved our understanding of galactic spiral shocks and their larger substructures, these studies have oversimplified the ISM thermodynamics, usually adopting an isothermal equation of state. This ignores potential consequences of thermal instability (TI; Field 1965; see also Meerson 1996 for a review), which changes an otherwise homogeneous ISM to clumpy, multiphase gas. (e.g., Field et al. 1969; Heiles 2001; Wolfire et al. 2003). In the classical two-phase picture of the ISM, cold dense clouds are in pressure equilibrium with the warm intercloud media that surround them (Field et al. 1969). Supernovae lead to a hot, diffuse third phase (Cox & Smith 1974; McKee & Ostriker 1977), but because massive star formation is spatially correlated and much of the hot gas produced is vented away, most of the volume remains relatively unaffected (e.g., Ferriere 1998; de Avillez & Breitschwerdt 2004). Since the cold clouds and the warm intercloud gas differ in density and temperature by about 2 orders of magnitudes, their respective responses to spiral shocks and downstream expansion flows will be much different from the isothermal case. When realistic thermal processes are considered, for instance, warm rarefied gas in the interarm region can be converted via shocks to cold dense gas in the arm regions. The reverse phase transition can then occur downstream for some fraction of the mass, yielding a quasi-steady cyclic exchange.

Shu et al. (1972) were the first to study the effects of gas cooling and heating on spiral shocks. By considering a mixture of the comoving two stable phases and allowing for phase transitions, they calculated steady state shock profiles for both cold and warm phases. However, they employed a pressure-density relation, instead of solving the time-dependent energy equation, based on the assumption of instantaneous thermal equilibrium; this precluded the possibility of unstable-phase gas in their calculations.

More recent years have seen a few numerical studies of spiral shocks with explicit heating and cooling, but most of these suffer from strong numerical diffusion. Baker & Barker (1974) argued that allowance for thermal phase changes produces "accretion fronts/waves" instead of spiral shocks, in which the inflowing material radiates its energy away. As they mentioned, however, this result could be due to large numerical diffusion; we will indeed show below that in a moving medium, numerical conductivity can be large enough to suppress TI. On the other hand, Tubbs (1980) and Marochnik et al. (1983) have shown that some models develop spiral shocks in which phase transitions from warm interarm gas to cold arm clouds occur, although insufficient resolution in their models made the cloud sizes and separations significantly overestimated and prevented the transition regions from cold to warm phases from being resolved. Very recently, Dobbs & Bonnell (2007) and Dobbs & Price (2008) studied the effects of the warm phase on a preexisting cold phase using particle simulations, but they did not allow for phase transitions that are crucial in spiral shocks with TI.

In this paper we initiate a study of galactic spiral shocks subject to ISM heating and cooling, using very high resolution numerical hydrodynamic simulations. We consider one-dimensional models that represent slices perpendicular to the arm. We ignore the gaseous self-gravity and magnetic fields here, deferring studies of these effects to future work. Our primary objectives are to determine overall shock structures under TI, to explore where and how the transitions among the cold, warm, and unstable phases occur, and to find statistical properties such as temperature distributions, mass fractions, and velocity dispersions.

The remainder of this paper is organized as follows. In § 2 we describe the basic equations we solve and present our model parameters and numerical methods. In § 3 we test our numerical code and quantify the diffusion (due to translational motion over the grid) in terms of a numerical conductivity. In § 4 we address the evolution of cold and warm phases as they traverse spiral shocks, and provide statistical measures to quantify the exchange cycle that develops. Finally, we summarize our results and discuss their implications in § 5.

2. NUMERICAL METHODS

2.1. *Basic Equations*

We study galactic gas flows and thermodynamic evolution in response to an external stellar spiral potential, which is assumed to be tightly wound with a pitch angle $i \ll 1$, and rotating at a constant pattern speed Ω_p with respect to an inertial frame. For local simulations, it is advantageous to set up a frame corotating with the spiral pattern, centered at the position $(R, \phi) = (R_0, \Omega_p t)$. The local frame is tilted by an angle i relative to the radial direction in such a way that the two orthogonal axes correspond to the directions perpendicular (x-axis) and parallel (y-axis) to the local arm segment (Roberts 1969). We assume that all physical variables depend only on the x-coordinate, while allowing nonzero velocity in the y-direction. Since the independent variable in our local models is a projection of the position on a streamline in a large-scale flow onto the x-axis, the distance on the x-axis divided by $\sin i$ represents the distance that the flow has traversed in the azimuthal direction along the streamline. Therefore, the *temporal* interval between one arm crossing and the next crossing is the same as it would be for a global model.

In the local arm frame, the background velocity due to galactic rotation is approximately given by

$$\boldsymbol{v}_0 = R_0(\Omega_0 - \Omega_p)\sin i\hat{\boldsymbol{x}} + [R_0(\Omega_0 - \Omega_p) - q_0\Omega_0 x]\hat{\boldsymbol{y}}, \tag{1}$$

where Ω_0 is the angular velocity of the gas at R_0 in the inertial frame and $q_0 \equiv -(d\ln\Omega/d\ln R)|_{R_0}$ is the local shear rate in the background flow in the absence of the spiral potential (Kim & Ostriker 2002, 2006). Assuming that the motions induced by the stellar potential are much smaller than $R_0\Omega_0$, the basic equations of ideal hydrodynamics expanded in the local frame read (see Roberts 1969; Shu et al. 1973; Balbus 1988; Kim & Ostriker 2002; Piontek & Ostriker 2004)

$$\frac{\partial\rho}{\partial t} + \nabla\cdot(\rho\boldsymbol{v}_T) = 0, \tag{2}$$

$$\frac{\partial\boldsymbol{v}_T}{\partial t} + \boldsymbol{v}_T\cdot\nabla\boldsymbol{v}_T = -\frac{1}{\rho}\nabla P - q_0\Omega_0 v_{0x}\hat{\boldsymbol{y}} - 2\boldsymbol{\Omega}_0\times\boldsymbol{v} - \nabla\Phi_{\rm ext}, \tag{3}$$

$$\frac{\partial e}{\partial t} + \boldsymbol{v}_T\cdot\nabla e = -\frac{\gamma}{\gamma-1}P\nabla\cdot\boldsymbol{v}_T - \rho\mathcal{L} + \nabla\cdot(\mathcal{K}\nabla T), \tag{4}$$

where $\boldsymbol{v}_T \equiv \boldsymbol{v}_0 + \boldsymbol{v}$ is the total velocity in the local frame, $\Phi_{\rm ext}$ is the external stellar spiral potential, $\rho\mathcal{L}(\rho, T)$ is the net cooling function, and $\mathcal{K}$ is the thermal conductivity. Other symbols have their usual meanings. We adopt an ideal gas law $P = (\gamma - 1)e$ with $\gamma = 5/3$.

For the stellar spiral potential, we consider a simple sinusoidal shape,

$$\Phi_{\rm ext} = \Phi_{\rm sp} \cos\left(\frac{2\pi x}{L_x}\right), \tag{5}$$

analogous to a logarithmic potential of Roberts (1969) and Shu et al. (1973). In equation (5), $\Phi_{\rm sp}$ denotes the amplitude of the spiral potential, while $L_x = 2\pi R_0 \sin i/m$ is the arm-to-arm separation for an m-armed spiral. We take the size of the simulation domain equal to L_x; since x varies from $-L_x/2$ to $L_x/2$ and $\Phi_{\rm sp} < 0$, $\Phi_{\rm ext}$ attains its minimum at the center ($x = 0$). We parameterize the spiral arm strength using

$$F \equiv \frac{m}{\sin i}\left(\frac{|\Phi_{\rm sp}|}{R_0^2\Omega_0^2}\right), \tag{6}$$

which measures the maximum force due to the spiral potential relative to the mean axisymmetric gravitational force (Roberts 1969).

The net cooling function per unit volume is given by $\rho\mathcal{L} \equiv n[n\Lambda(T) - \Gamma]$, where $n = \rho/(\mu m_{\rm H})$ is the gas number density and $\mu = 1.27$ is the mean molecular weight per particle. For the heating and cooling rates of the atomic ISM, we take the fitting formulae

$$\Gamma = 2.0 \times 10^{-26} \text{ erg s}^{-1}, \tag{7}$$

$$\frac{\Lambda(T)}{\Gamma} = 10^7 \exp\left(\frac{-1.184\times 10^5}{T + 1000}\right) + 1.4\times 10^{-2}\sqrt{T}\exp\left(\frac{-92}{T}\right) \text{ cm}^3, \tag{8}$$

suggested by Koyama & Inutsuka (2002; see also Vázquez-Semadeni et al. 2007). Under the adopted net cooling curve, the minimum and maximum pressures for the coexistence of the classical warm/cold phases in a static equilibrium are $P_{\rm min}/k_{\rm B} = 1600$ K cm^{-3} and $P_{\rm max}/k_{\rm B} = 5000$ K cm^{-3}. The corresponding transition temperatures $T_{\rm max} = 5012$ K and $T_{\rm min} = 185$ K define cold ($T < T_{\rm min}$), warm ($T > T_{\rm max}$), and intermediate-temperature phases ($T_{\rm min} < T < T_{\rm max}$). To resolve the length scales of TI numerically (e.g., Koyama & Inutsuka 2004; Piontek & Ostriker 2004), we include a constant value of thermal conductivity $\mathcal{K}_0 = 10^5$ erg s^{-1} cm^{-1} K^{-1}.[3] The associated Field length below which thermal conduction erases temperature perturbations completely is defined by (Field 1965)

$$\lambda_{\rm F} = 2\pi\left\{\frac{\rho^2\Lambda}{\mathcal{K}_0 T}\left[1 - \left(\frac{\partial \ln \Lambda}{\partial \ln T}\right)\right]\right\}^{-1/2}. \tag{9}$$

In our models, $\lambda_{\rm F}$ typically amounts to $\sim$0.18 pc.

2.2. *Model Parameters and Numerical Methods*

We consider a simulation box in which the gas is initially homogeneous with density n_0 and pressure P_0 when a spiral perturbation is absent. Other than thermal processes involving TI, the overall dynamics and structures of spiral shocks in our models are completely characterized by the arm-to-arm distance L_x and the flow speed v_{0x} relative to the perturbing stellar potential in the x-direction (as well as $\sin i$, q_0, F, and Ω_p/Ω_0). The azimuthal wavenumber m of spiral arms is arbitrary, and the box location and the gaseous angular speed relative to the arms can then be specified as $R_0 = mL_x/(2\pi \sin i)$ and $\Omega_0 - \Omega_p = 2\pi v_{0x}/(mL_x)$, respectively. To achieve the numerical resolution sufficient to resolve the Field length, we consider a small box with $L_x = 628$ pc. For the relative velocity, we choose $v_{0x} = 13$ km s^{-1} corresponding to the rotational velocity of $R_0\Omega_0 = 260$ km s^{-1} with a flat rotation curve ($q_0 = 1$). The corresponding arm-to-arm crossing time is $t_{\rm cross} \equiv L_x/v_{0x} = 4.7 \times 10^7$ yr, which we choose as the fiducial time unit in our presentation. For spiral arm parameters, we take pattern speed $\Omega_p = \Omega_0/2$, pitch angle $\sin i = 0.1$, and strength $F = 5\%$ in all the models. We note that, driven by the numerical requirement, spiral arms in our models have a small separation and thus a short dynamical time, so that some of our numerical results (e.g., mass fractions) that depend on the ratio of cooling time to dynamical time may not be applicable to spiral arms with a much larger arm-to-arm crossing time.

To simulate spiral shocks with varying total gas contents, we consider 12 models that have the same initial thermal pressure $P_0/k_{\rm B}$ but differ in the initial density n_0; we adopt the solar neighborhood value at $P_0/k_{\rm B} = 3000$ K cm^{-3} based on the observational (e.g., Ferriere 2001; Heiles & Troland 2003; Jenkins & Tripp 2007) and theoretical (e.g., Wolfire et al. 2003) arguments. Note that although some models are out of thermal equilibrium initially, they immediately tend toward equilibrium owing to rapid heating and cooling, with the equilibrium pressure depending on n_0. Table 1 lists the model parameters and simulation outcomes. Column (1) labels each run; while the models with the prefix SU rapidly undergo TI even with $F = 0$, the SW and SC models would stay warm or cold throughout were it not for the spiral perturbations. Column (2) lists n_0. Columns (3)–(8) give the width of, and time spent in, the arm, transition, and interarm regions, respectively, in each model. The mass and volume fractions of the cold, warm, and intermediate-temperature phases are given in columns (9)–(14), respectively. We take model SU2 with $n_0 = 2$ cm^{-3} as our fiducial model; at this density, the total surface density would be $\sim$12 $M_\odot$ pc^{-2} for a vertical scale height of $\sim$100 pc.

We integrate the time-dependent partial differential equations (2)–(4) using a modified version of the Athena code (Gardiner & Stone 2005). Athena implements a single-step, directionally unsplit Godunov scheme for compressible hydrodynamics in multispatial dimensions and allows a variety of spatial reconstruction methods and approximate Riemann solvers; the version we use here employs the piecewise linear method (PLM) with the Roe Riemann solver.[4] We implement the shearing-periodic boundary condition at the x-boundaries (Hawley et al. 1995). Because of the very short cooling time, energy updates from net cooling are made implicitly based on Newton-Raphson iteration, while the conduction term is solved fully explicitly. For stable and accurate results, we ensure the time step is kept smaller than the CFL condition for thermal conduction as well as the cooling/heating time (see Piontek & Ostriker 2004). Our standard models employ $N = 16{,}384$ zones, corresponding to grid spacing of $\Delta x = 0.04$ pc, which satisfies the condition $\Delta x < \lambda_{\rm F}/3$ for the convergence of numerical results (Koyama &

---

[3] While thermal conductivity is proportional to $T^{1/2}$ for neutral hydrogen at kinetic temperatures below 4.5×10^4 K (Parker 1953), we choose for simplicity a fixed value corresponding to thermal equilibrium at $T = 1500$ K for our standard density $n_0 = 2$ cm^{-3}.

[4] Although the piecewise parabolic method (PPM) is known to provide, in general, less diffusive spatial reconstruction than the PLM, our experiments have shown that the PPM often produced negative internal energy in the presence of strong radiative cooling inside spiral shocks.

TABLE 1

Summary of Model Parameters and Simulation Results

		Arm		Transition		Interarm		Mass Fractions (%)			Volume Fractions (%)		
Model (1)	n_0 (2)	$\Delta L/L_x$ (3)	$\Delta t/t_{\rm cross}$ (4)	$\Delta L/L_x$ (5)	$\Delta t/t_{\rm cross}$ (6)	$\Delta L/L_x$ (7)	$\Delta t/t_{\rm cross}$ (8)	Cold (9)	Intermediate (10)	Warm (11)	Cold (12)	Intermediate (13)	Warm (14)
SW0.1	0.1	...	...	...	...	...	...	0	0	100	0	0	100
SW0.5	0.5	0.00	0.05	0.04	0.14	0.96	0.82	18	26	55	0	10	90
SW1	1.0	0.00	0.10	0.10	0.21	0.89	0.69	43	25	31	2	16	83
SU2	2.0	0.01	0.14	0.16	0.22	0.83	0.64	59	27	14	4	26	70
SU3	3.0	0.01	0.16	0.22	0.24	0.77	0.60	62	30	8	7	35	58
SU4	4.0	0.02	0.19	0.26	0.25	0.72	0.56	65	29	5	11	40	49
SU5	5.0	0.03	0.20	0.28	0.25	0.69	0.54	66	30	3	14	43	43
SU6	6.0	0.04	0.22	0.32	0.28	0.63	0.50	67	31	2	18	48	34
SU7	7.0	0.05	0.23	0.35	0.30	0.60	0.47	70	29	2	23	47	30
SU8	8.0	0.06	0.24	0.35	0.29	0.59	0.47	73	26	1	29	45	26
SC10	10.0	0.08	0.27	0.40	0.32	0.52	0.41	76	24	1	37	46	17
SC20	20.0	...	...	...	...	...	...	100	0	0	100	0	0

Note.—Col. (1): Model name; Col. (2): Initial number density in units of cm^{-3}; Cols. (3)–(8): Width and duration of the arm, transition, and interarm regions; Cols. (9)–(14): Mass and volume fractions of the cold, intermediate-temperature, and warm phases.

Inutsuka 2004); we also ran models with different grid sizes in order to study the effects of numerical resolution.

3. CODE TESTS AND NUMERICAL CONDUCTIVITY

The Athena code we use has been verified on a wide variety of test problems including hydrodynamic shock tubes, advection of a square box in a background shear flow, and one-dimensional propagation of sound waves in a rotating, shearing medium. For simulations involving cooling/heating and conduction terms, it is crucial to check if the numerical scheme employed can resolve the length scales and timescales of the fastest growing TI modes. This test is of particular importance for the current work since the gas in our models is nonstatic, moving in the x-direction at an average speed of $v_{0x} = 13$ km s^{-1}, so that numerical diffusion associated with advection and zone averaging may reduce the growth rates of TI at small scales. In this section, we describe the test results of our numerical code on the development of TI in static, rotating, and moving media in the absence of spiral potential perturbations and provide a quantitative measure of the numerical diffusion in terms of numerical conductivity.

3.1. *Linear Dispersion Relation*

We test our code by comparing the numerical growth rate of a particular TI mode with the corresponding analytic prediction. To this end, we derive a dispersion relation for local, axisymmetric TI in a homogeneous medium that is rotating, shearing, and undergoing uniform translational motion with $\boldsymbol{v}_0$. We linearize equations (2)–(4) (dropping the external potential), assuming plane-wave disturbances $\propto e^{nt-ikx}$, where n and k are the growth rate and wavenumber of the disturbances in the x-direction, respectively. We follow the same steps as in Field (1965), except that we include the nonzero background motions and the indirect forces arising from galaxy rotation. The resulting dispersion relation for local disturbances is given by

$$\tilde{n}^3 + \tilde{n}^2 a\left(k_T + \frac{k^2}{k_\mathcal{K}}\right) + \tilde{n}\left(\kappa^2 + k^2a^2\right) + a\left[\frac{a^2k^2}{\gamma}\left(k_T - k_\rho + \frac{k^2}{k_\mathcal{K}}\right) + \kappa^2\left(k_T + \frac{k^2}{k_\mathcal{K}}\right)\right] = 0, \quad (10)$$

where $\tilde{n} \equiv n - ikv_{0x}$ is the Doppler-shifted growth rate, $a \equiv (\gamma k_{\rm B}T/\mu m_{\rm H})^{1/2}$ is the adiabatic speed of sound, $\kappa \equiv [R^{-3}d(R^4\Omega^2)/dR|_{R_0}]^{1/2} = (4-2q_0)^{1/2}\Omega_0$ is the local epicyclic frequency, and k_T, k_ρ, and $k_\mathcal{K}$ are the wavenumbers defined by (e.g., Field 1965)

$$k_T = \frac{\gamma(\gamma-1)}{a^3}\left(\frac{\partial\mathcal{L}}{\partial\ln T}\right)_\rho, \quad k_\rho = \frac{\gamma(\gamma-1)}{a^3}\left(\frac{\partial\mathcal{L}}{\partial\ln\rho}\right)_T,$$
$$k_\mathcal{K} = \frac{a^3\rho}{\gamma(\gamma-1)\mathcal{K}T}. \quad (11)$$

In the limit of $q_0 = 0$ and $v_{0x} = 0$, equation (10) recovers the dispersion relation given by Field (1965) for TI in a rigidly rotating medium with no translational motion. The fact that v_{0x} occurs in the dispersion relation only through $\tilde{n}$ implies that a constant translational motion does not change the growth rates of TI if measured in a frame moving with v_{0x}, analogous to Galilean invariance in mechanics.

For isobaric TI to occur, the term in the square brackets in equation (10) must be negative. This of course necessitates $k_T - k_\rho < 0$, the Field criterion for isobaric TI (Field 1965). Thermal conduction and rotation suppress short- and long-wavelength perturbations against TI, respectively, reducing the unstable range of wavelengths to $k_1 < k < k_2$, where k_1 and k_2 are two positive roots of $k^4 + [k_\mathcal{K}(k_T - k_\rho) + \gamma\kappa^2/a^2]k^2 + \gamma\kappa^2k_Tk_\mathcal{K}/a^2 = 0$. One can show that $k_2 \rightarrow [k_\mathcal{K}(k_\rho - k_T)]^{1/2} = 2\pi/\lambda_{\rm F}$ for weakly rotating or nonrotating systems ($\kappa \rightarrow 0$), while $k_1^2 \rightarrow \gamma\kappa^2k_T/[a^2(k_\rho - k_T)]$ in the limit of vanishingly small conductivity ($k_\mathcal{K} \rightarrow \infty$). Figure 1 plots as various lines sample growth rates $\tilde{n}$ of TI calculated from equation (10) for cases $\mathcal{K} = \Omega_0 = 0$ (*dotted line*), $\mathcal{K} = \mathcal{K}_0$ with $\Omega_0 = 0$ (*solid line*), and $\mathcal{K} = \mathcal{K}_0$ with $\Omega_0 = 130$ km s^{-1} kpc^{-1} (*dashed line*). The density, pressure, and shear parameter are taken to be $n_0 = 2$ cm^{-3}, $P_0/k_{\rm B} = 3000$ cm^{-3}, and $q_0 = 1$, respectively, corresponding to our fiducial model SU2. Stabilization of TI by rotation and conduction is apparent at large and small scales, causing the wavelengths of the most unstable disturbances to occur at $\lambda \sim 3$ pc in between the cutoff wavelengths.

3.2. *Numerical Conductivity*

For our code tests, we consider three kinds of models depending on Ω_0 and Ω_p: (1) a static disk ($\Omega_0 = \Omega_p = 0$); (2) a rotating

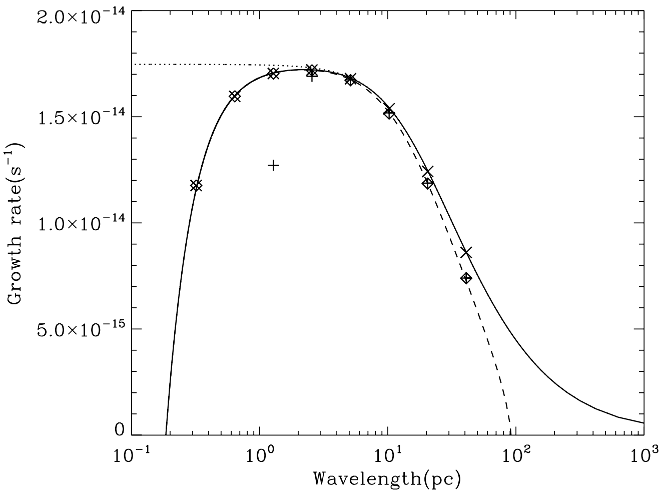

FIG. 1.—Analytic growth rate of TI vs. perturbation wavelength (eq. [10]) for cases $\mathcal{K} = \Omega_0 = 0$ (*dotted line*), $\mathcal{K} = \mathcal{K}_0$ with $\Omega_0 = 0$ (*solid line*), and $\mathcal{K} = \mathcal{K}_0$ with $\Omega_0 = 130$ km s^{-1} kpc^{-1} (*dashed line*), showing that rotation and conduction stabilize perturbations at large and small scales, respectively. Symbols indicate the numerical growth rates measured from test simulations, all with $\mathcal{K} = \mathcal{K}_0$, for a static medium (*crosses*), for a rotating medium without translational motion (*diamonds*), and for a medium with both rotational and translational motion (*plus signs*). Note that numerical diffusion associated with translational motion over the grid reduces the growth rates at small scales significantly. See text for details.

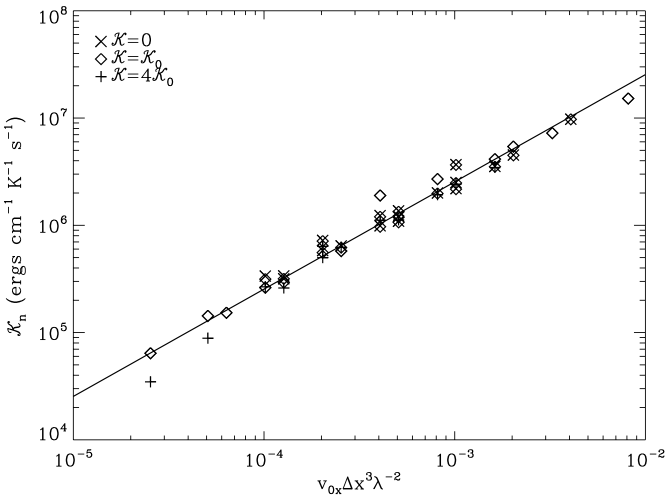

FIG. 2.—Dependence of numerical conductivity $\mathcal{K}_n$ on the translational velocity v_{0x}, the grid size Δx, and the perturbation wavelength λ of TI, from the test simulations with physical conductivity $\mathcal{K} = 0$ (*crosses*), $\mathcal{K} = \mathcal{K}_0$ (*diamonds*), and $\mathcal{K} = 4\mathcal{K}_0$ (*plus signs*). Note that v_{0x} is expressed in units of km s^{-1}, while Δx and λ are in parsecs. The solid line, represented by eq. (12), gives the best fit to the test results based on the second-order PLM for spatial reconstruction in the Athena code we use.

disk without translational motion ($\Omega_0 = \Omega_p = 130$ km s^{-1} kpc^{-1}, yielding $v_{0x} = 0$ from eq. [1]); and (3) a rotating disk with translational motion ($\Omega_0 = 2\Omega_p = 130$ km s^{-1} kpc^{-1}, so that $v_{0x} = 13$ km s^{-1}). The same conductivity $\mathcal{K} = \mathcal{K}_0$ is adopted for all the models. Other parameters including n_0, P_0, and q_0 are the same as in model SU2. In each model, we initialize an eigenmode of TI with wavelength λ and vary the box size to fit it in, while keeping the grid spacing $\Delta x = 0.04$ pc fixed. We monitor the evolution of the maximum density and measure its growth rate numerically in the linear regime. Figure 1 plots the resulting growth rates from the runs as crosses, diamonds, and plus signs for the first, second, and third types of models, respectively. Evidently, the numerical and analytic results are in good agreement for models without the translational motion, confirming the performance of our implementation of the heating/cooling and conduction terms. While the translational motion of the gas at a level of $v_{0x} = 13$ km s^{-1} does not affect large-scale modes much, it significantly reduces the numerical growth rates for small-scale modes with $\lambda < 2$ pc. The discrepancy between the numerical and analytic results appear to be due to numerical diffusion that causes the thermal energy to spread out as cooling/heating regions are advected with the background flow.

To quantify the strength of numerical heat diffusion in our code, we solve the linear dispersion relation (10) for a given set of parameters to find the effective conductivity $\mathcal{K}_{\rm eff}$ that yields an analytic growth rate equal to the numerical value obtained from the model simulation with the same parameters except for the physical conductivity $\mathcal{K} = \mathcal{K}_0$. We then calculate the numerical conductivity from $\mathcal{K}_n = \mathcal{K}_{\rm eff} - \mathcal{K}$. In the case of models with $v_{0x} = 13$ km s^{-1} and $\lambda = 2.56$ and 1.28 pc shown in Figure 1, for instance, $\mathcal{K}_n = 3.4 \times 10^5$ and 1.2×10^6 erg s^{-1} cm^{-1} K^{-1}, respectively, about 3.4 and 12 times larger than $\mathcal{K}_0$.

In order to find the parametric dependences of $\mathcal{K}_n$ on the translational velocity, grid size, and perturbation wavelength, we ran a suite of models varying v_{0x} from 2.6 to 26 km s^{-1}, Δx from 0.02 to 0.16 pc, and λ from 0.32 to 10.2 pc. We also explored the cases with different levels of physical conductivity at $\mathcal{K} = 0$, $\mathcal{K}_0$, or $4\mathcal{K}_0$. The numerical conductivity is calculated only when the numerical growth rate is lower than the analytic value at the same $\mathcal{K}$ by more than 1%. Figure 2 plots as various symbols the resulting numerical conductivity based on the PLM scheme for spatial reconstruction, showing that $\mathcal{K}_n$ is well fitted by

$$\mathcal{K}_n = 10^{9.4} \frac{v_{0x}}{1 \text{ km s}^{-1}} \left(\frac{\Delta x}{1 \text{ pc}}\right)^3 \left(\frac{\lambda}{1 \text{ pc}}\right)^{-2} \text{ erg s}^{-1} \text{ cm}^{-1} \text{ K}^{-1}. \tag{12}$$

This suggests that the numerical conductivity in a moving medium depends rather sensitively on the numerical resolution. Equation (12) states that our models with $\Delta x = 0.04$ pc have numerical conductivity comparable to the physical conductivity for the fastest growing modes, so that the effect of numerical diffusion on the results presented in this paper is not significant.

We repeated the same calculations using the higher order piecewise parabolic method (PPM) reconstruction scheme and found that the numerical conductivity is linearly proportional to $v_{0x}\Delta x^4\lambda^{-3}$. Generalizing these results, we rewrite equation (12) as $\mathcal{K}_n \propto v_{0x}\Delta x(\Delta x/\lambda)^p$, where p is the order of the spatial reconstruction scheme ($p = 2$ and 3 for PLM and PPM, respectively). This implies that the numerical conductivity can be viewed as a diffusion coefficient ($\propto v_{0x}\Delta x$) modified by the accuracy of the interpolation scheme used in spatial reconstruction [$\propto(\Delta x/\lambda)^p$].

4. NONLINEAR SIMULATIONS

4.1. *Standard Model*

We now study the nonlinear evolution of thermally unstable gas flows under an imposed spiral potential. In this subsection we focus on model SU2 with $n_0 = 2$ cm^{-3}. We initially apply density perturbations created by a Gaussian random field with a power spectrum $|\rho_k|^2 \propto k^{-5/3}$ for $1 \le 2\pi k/L_x \le 128$ and zero power for $2\pi k/L_x > 128$ in the Fourier space, corresponding to a one-dimensional Kolmogorov spectrum for sonic disturbances. The standard deviation of the density perturbations is fixed to be 1% in physical space. In order to suppress rapid motions of the

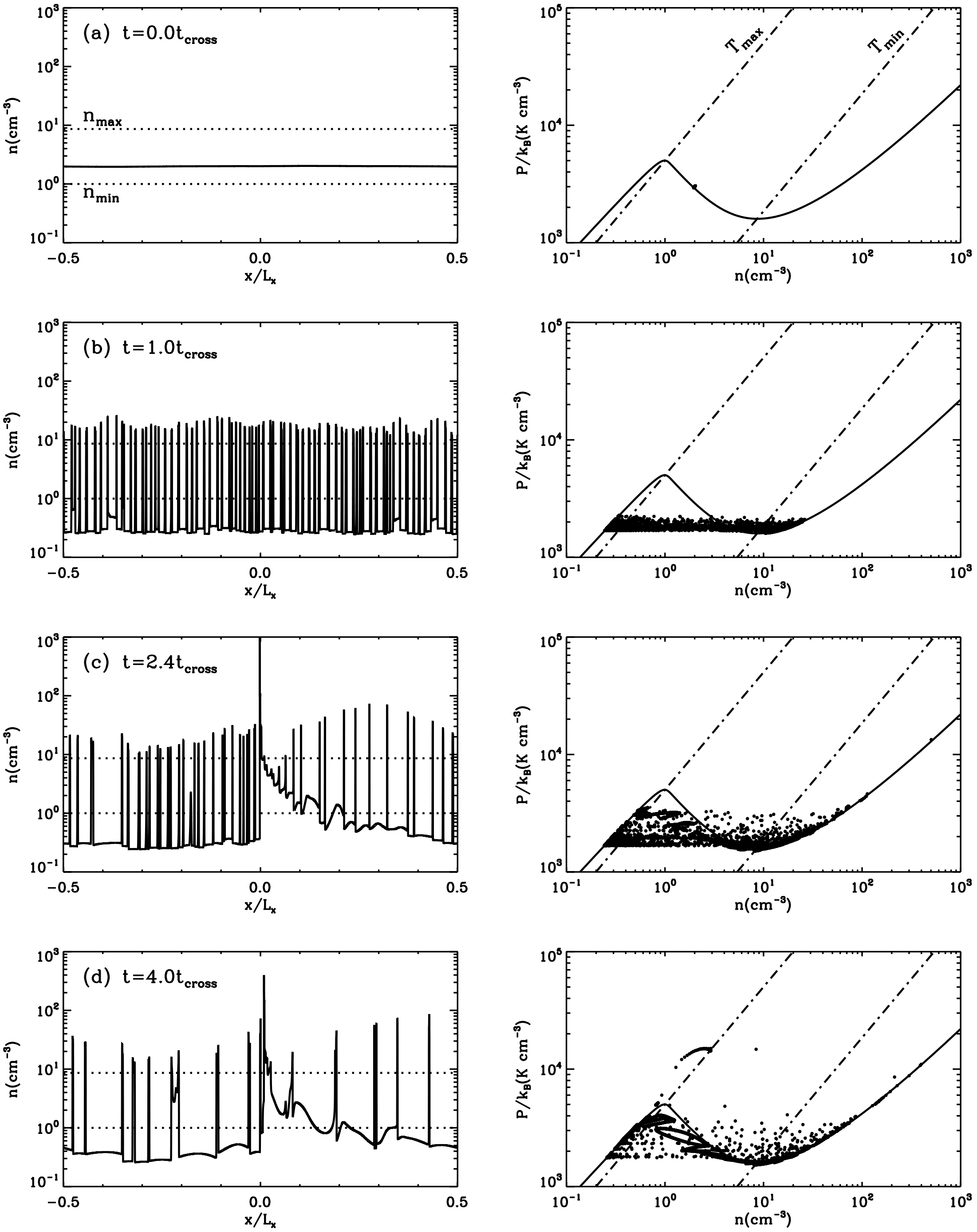

FIG. 3.—*Left*: Density snapshots at $t/t_{\rm cross} = 0.0, 1.0, 2.4$, and 4.0 from model SU2. Dotted lines labeled by $n_{\rm max}$ and $n_{\rm min}$ demarcate the cold and warm phases. *Right*: Corresponding scatter plots of n vs. $P/k_{\rm B}$ together with the equilibrium cooling curve (*solid lines*). Dot-dashed lines marked by $T_{\rm max}$ and $T_{\rm min}$ divide the warm ($T > T_{\rm max}$), intermediate-temperature ($T_{\rm min} < T < T_{\rm max}$), and cold ($T < T_{\rm min}$) phases.

gas caused by an abrupt introduction of the spiral potential, we slowly turn it on, reaching the full level $F = 5\%$ at $t/t_{\rm cross} \sim 2.4$.

Figure 3 shows density distributions of model SU2 at $t/t_{\rm cross} = 0$, 1, 2.4, and 4.0 together with scatter plots of pressure versus density overlaid on the equilibrium cooling curve. The gas initially has $T = 1500$ K and is thus thermally unstable (Fig. 3*a*). It evolves rapidly to cold ($n > n_{\rm max} = 8.6$ cm^{-3} and $T < T_{\rm min} = 185$ K) and warm ($n < n_{\rm min} = 1$ cm^{-3} and $T > T_{\rm max} = 5012$ K) phases within $0.5t_{\rm cross}$. The TI soon saturates, and random cloud motions aided by epicyclic shaking cause cold clouds to collide and merge together, or split sometimes, resulting in, on average, 70 cold clouds with a mean cloud separation of ~0.8 pc, which are in rough pressure equilibrium with the surrounding warm gas at $P/k_{\rm B} = 1900$ K cm^{-3} (Fig. 3*b*). At this time, the spiral potential remains weak and most gas in the unstable temperature range corresponds to the boundaries of the cold clouds. As the amplitude of the potential grows, the gas is gathered toward the potential minimum, forming a spiral shock near $x = 0$. The shock reaches maximum strength at around $t/t_{\rm cross} = 2.5$ shortly after F attains the full strength. Both cold and warm phases in the interarm regions continually enter the shock front and are compressed to become cold gas with higher density. They subsequently expand

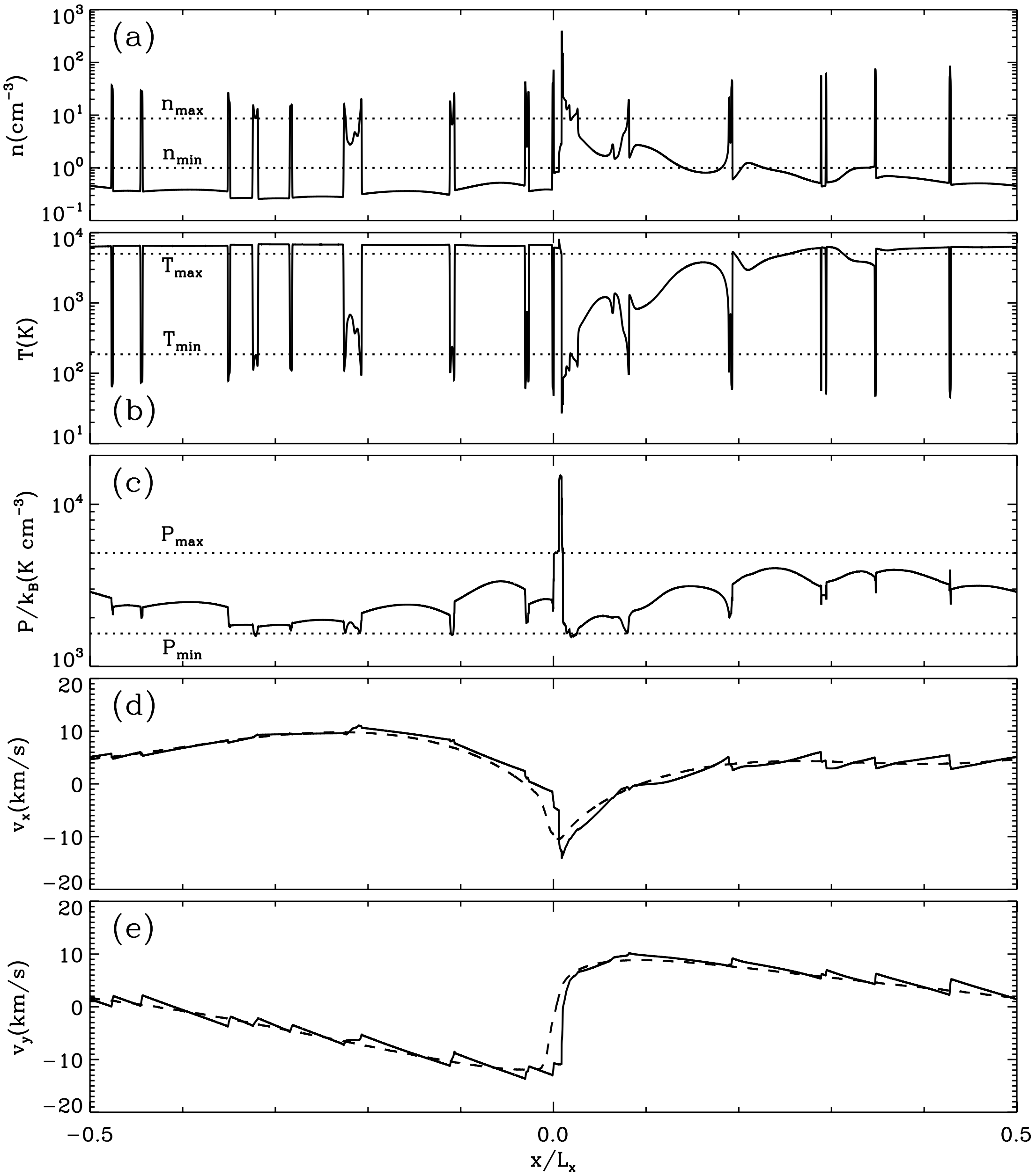

FIG. 4.—Profiles of number density, temperature, pressure, and perturbation components of the velocities perpendicular ($v_x = v_{T,x} - v_{0x}$) and parallel ($v_y = v_{T,y} - v_{0y}$) to the arm, for model SU2 at $t/t_{\rm cross} = 4.0$. In (*a–c*), dotted lines demark the transitions between the cold, intermediate-temperature, and warm phases. Dashed lines in (*d*) and (*e*) show the time-averaged velocity (streaming) profiles over $t/t_{\rm cross} = 5$–8.

and become thermally unstable as they leave the spiral arm regions, returning back to the cold and warm interarm phases (see below). At about $t/t_{\rm cross} = 3$, the overall shock structure reaches a quasi-steady state in the sense that the mass and volume fractions of each phase do not change appreciably with time, although the shock oscillates slightly around an equilibrium position and cold clouds shift as they follow galaxy rotation (projected onto the $\hat{x}$-direction).

Figure 4 plots the distributions of physical variables in model SU2 at $t/t_{\rm cross} = 4$ after this quasi-steady state has been reached; many spikes and discontinuities in density as well as sawtooth-like velocity profiles are evident. Figure 5 schematically illustrates the evolutionary tracks of the cold and warm phases in the *n*-*P* plane. Regions marked with A, B, C, and D correspond to interarm, immediate postshock, spiral arm, and thermally unstable transition zones, respectively; the transition zone refers to the window downstream from the arm (between $x/L_x \sim 0.03$ and 0.2) in Figure 4*b*, where most of the gas has temperatures in the unstable range between $T_{\rm min}$ and $T_{\rm max}$. The subscripts 1 and 2 denote the warm and cold phases, respectively, of interarm gas and their respective immediate postshock counterparts.

In the interarm regions (either $x/L_x < 0$ or $x/L_x > 0.2$ in Fig. 4), warm (A_1) and cold (A_2) phases are in rough equilibrium in terms of the total (=thermal + ram) pressure. While the cold interarm clouds typically have slightly lower thermal pressure than the warm interarm medium, their ram pressure is of comparable magnitude, i.e., $P/k_{\rm B} \sim 2000$–4000 K cm^{-3}. Some of the cold interarm clouds exhibit "double-horned" structure, a consequence of merging with neighbors or splitting into two pieces (see, e.g., Fig. 4*a*). As the warm and cold interarm phases enter the shock front, they experience a strong compression, jumping to B_1 and B_2, respectively. While the density jump is by a factor of 4 for both cold and warm phases, the pressure jump for the cold phase is

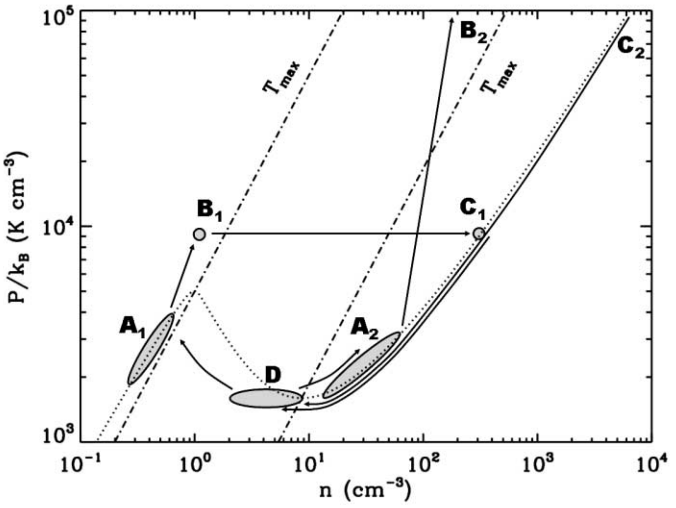

FIG. 5.—Schematic evolutionary track in the *n-P* plane (*solid lines with arrows*) of gas cycling through a spiral pattern with TI. The dotted line is the thermal equilibrium curve, while dot-dashed lines mark $T_{\rm max}$ and $T_{\rm min}$. The warm and cold phases in the interarm regions (A) are shocked (B), undergo radiative cooling (C), become thermally unstable due to postshock expansion (D), and return to the interarm two-phase state again (A). See text for details.

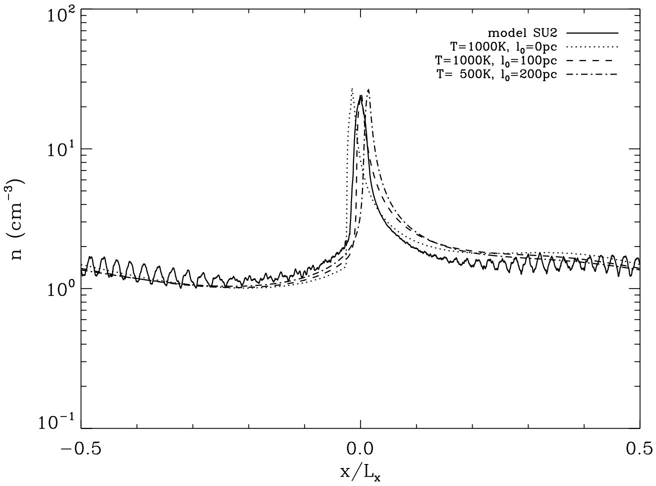

FIG. 6.—Density profile averaged over $t/t_{\rm cross} = 5$–8 from model SU2 (*solid line*), compared to stationary shock profiles for isothermal models, the $T = 1000$ K nonviscous model (*dotted line*), the $T = 500$ K viscous model with $l_0 = 200$ pc (*dot-dashed line*), and the $T = 1000$ K viscous model with $l_0 = 100$ pc (*dashed line*).

about 10 times larger than in the warm phase since the former is about 100 times colder.[5] The shocked gas in states B_1 and B_2 is not in thermal balance and subsequently undergoes strong postshock cooling (e.g., Mufson 1974), moving almost isobarically to C_1 and C_2. The transition from A to C is essentially instantaneous (cooling time $\sim 10^3$ yr).[6]

One of the characteristics of galactic spiral shocks is that gas accelerates after the maximum shock compression (e.g., Roberts 1969; Balbus 1988; Kim & Ostriker 2002). Because of this postshock expansion, the cold gas inside the arm ($0 < x/L_x < 0.03$) becomes progressively less dense, evolving from C to D. Since the dynamical timescale is much longer than the cooling time (due to the reduced velocity inside the arm), the cold gas either at C_1 or C_2 moves all the way down to the transition zone D following the equilibrium curve in the *n-P* plane. When the expanding gas reaches region D ($0.03 < x/L_x < 0.2$), it becomes thermally unstable and turns back into either the warm (A_1) or cold (A_2) interarm phase. For model SU2, it typically takes about $\sim 0.14 t_{\rm cross}$ from C to D stages and $\sim 0.22 t_{\rm cross}$ from D to A stages. Gas is in the interarm regime A for the balance of the cycle ($\sim 0.64 t_{\rm cross}$). When averaged over $t/t_{\rm cross} = 5-8$, the arm, transition, and interarm regions in model SU2 occupy approximately 1%, 16%, and 83% of the spatial domain, respectively.

Our models, as well as the real ISM, contain many interarm clouds which would be too small to be detected individually in extragalactic radio observations. In modeling gaseous spiral shocks, Lubow et al. (1986) did not explicitly solve for the cloudy structure. Instead, they adopted an isothermal equation of state and treated the effects of cold clouds (and their collisions) by including a viscous term parameterized by a mean free path l_0 for the fluid. They found that viscosity renders arm profiles smoother and more symmetric. In order to compare our models with a single-phase viscous counterpart, we take a temporal average over $t/t_{\rm cross} = 5$–8 of the density distributions in model SU2. We then take a boxcar average of the time-averaged profile, with a window of 8 pc. Figure 6 plots the resulting mean density profile as a solid line. For comparison, we have run isothermal models that include an explicit viscosity term in the momentum equation (3) in a manner similar to that in Lubow et al. (1986). Selected results are shown in Figure 6. Evidently, larger viscosity tends to produce a weaker spiral shock, with a peak that is more symmetric and farther downstream. In terms of the strength and placement of the spiral arm, an isothermal model with $T = 1000$ K and $l_0 = 100$ pc provides a fairly good match for the mean density profile when TI is included. The isothermal viscous model, however, has a slightly broader arm compared to the time average of the multiphase model. Our results thus demonstrate that (for the purposes of obtaining a lower resolution "beam-averaged" profile) the effects of clouds embedded in a warm medium can be effectively modeled by viscosity (Cowie 1980; Gammie 1996), but only if the medium's temperature and the mean free path are chosen appropriately. We note that if a temperature comparable to that of the warm medium were adopted for an isothermal counterpart, the shock would generally be too weak.

4.2. *Effects of Initial Number Density*

All the SU models we consider start from a thermally unstable initial state. Since the TI growth time is short compared to the time over which we turn on the spiral potential, these models first evolve into a thermally bistable state before developing shocks. Figure 7 plots a density profile at $t/t_{\rm cross} = 4$ in model SU5 with $n_0 = 5$ cm^{-3}. Comparing to model SU2 as shown in Figure 3, Figure 7 shows that the densities (and temperatures) of the cold and warm phases after TI saturates are insensitive to the initial gas density, although of course models with higher n_0 produce more cold clumps.[7] The ensuing development of spiral shocks and evolutionary tracks in the *n-P* plane are also qualitatively similar to those described in § 4.1.

---

[5] Strictly speaking, this holds true only for one-dimensional shocks. In two or three dimensions, small clouds can experience enhanced compression as the shock wrapping around them is able to propagate toward the cloud centers. They may also be subject to dynamical effects such as Kelvin-Helmholtz and Rayleigh-Taylor instabilities (e.g., Woodward 1976).

[6] Because of its very large postshock density, the transition from A_2 to C_2 occurs over an extremely short cooling scale (~ 0.02 pc) that is not resolved in our models.

[7] Mass conservation requires the number of cold clouds N_c to be given approximately by $N_c \approx n_0 L_x/(l n_c)$, where l and n_c are the mean size and number density of the clouds. From simulations with differing n_0, we empirically found that $l \sim 0.8$ pc $(n_0/2\ {\rm cm}^{-3})^{0.3}$, i.e., the mean cloud size (presumably set by merging and splitting), depends only weakly on n_0. This gives $N_c \propto n_0^{0.7}$.

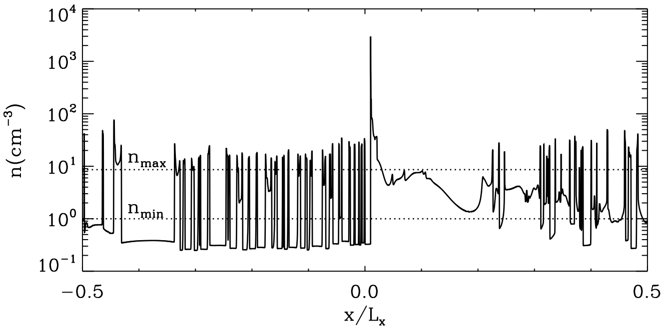

FIG. 7.—Density profile of model SU5 with $n_0 = 5$ cm^{-3} at $t/t_{\rm cross} = 4$. Note that the postshock transition zone in model SU5 is wider than that of model SU2 shown in Fig. 4.

Perhaps the most notable difference in the late-time states with different n_0 is the size of the postshock transition zone. Columns (3)–(8) of Table 1 show that the transition zone (and also the arm region, to a lesser extent) widens with increasing n_0. One can easily see this by comparing Figures 4*a* and 7. This trend is of course because models with larger n_0 have a larger fraction of the total mass in the cold phase that evaporates to maintain an unstable state. In addition, the mean separation of cold clouds inside the arm is smaller in models with higher n_0, allowing for merging with neighboring clouds more often during the postshock expansion stage. This reduces the expansion rate effectively, thereby extending the size of zones with unstable density toward downstream.

Unlike the SU models, the SW and SC models initially have a low or high enough density that they are thermally stable and the early development of a spiral shock takes place in a single-phase medium. Nevertheless, the shock compression and/or postshock expansion can still produce thermally unstable gas if the initial density is not far from the unstable range. For example, the shock in model SW0.5 drives the thermal pressure above $P_{\rm max}$, and the gas evolves rapidly via TI into a cold stable phase inside the arm. In model SC10, on the other hand, strong postshock expansion drives the pressure of the initially cold gas below $P_{\rm min}$, after which a fraction of the gas expands to become a warm phase. Consequently, the resulting structures at late times in models SW0.5 and SC10 are similar to those in the SU models. In models with n_0 further away from the unstable values, however, changes in the gas pressure due to shock compression and postshock expansion are insufficient to trigger phase transitions. Figure 8 plots equilibrium shock profiles in models SW0.1 and SC20, which start with $n_0 = 0.1$ and 20 cm^{-3}, respectively. The gas in both of these models consists only of the warm or cold phase and the profiles are smooth everywhere except at the shock front.

4.3. *Temperature Distribution*

Figure 9 plots the volume-weighted and mass-weighted temperature probability distribution functions (PDFs) for models SW0.5, SU2, SU5, and SC10, averaged over $t/t_{\rm cross} = 5-8$. The vertical dotted lines in each panel indicate $T_{\rm min}$ and $T_{\rm max}$, marking the cold, intermediate-temperature, and warm phases. For the standard model SU2, the mass-weighed temperature PDF is characterized by a broad cold peak at $T \sim 20-150$ K and a narrow warm peak at $T \sim 6000-8000$ K, although there also exists a substantial amount of the intermediate-temperature gas. In the broad cold peak, the portion of gas with $T \lesssim 50$ K corresponds to the very dense arm population immediately behind the shock, while the portion with 50 K $\lesssim T < T_{\rm min}$ includes both arm and interarm cold clouds. Since a larger initial density implies a larger initial cold fraction even before the spiral potential is applied, the cold mass fractions in both arm and interarm regions increase in

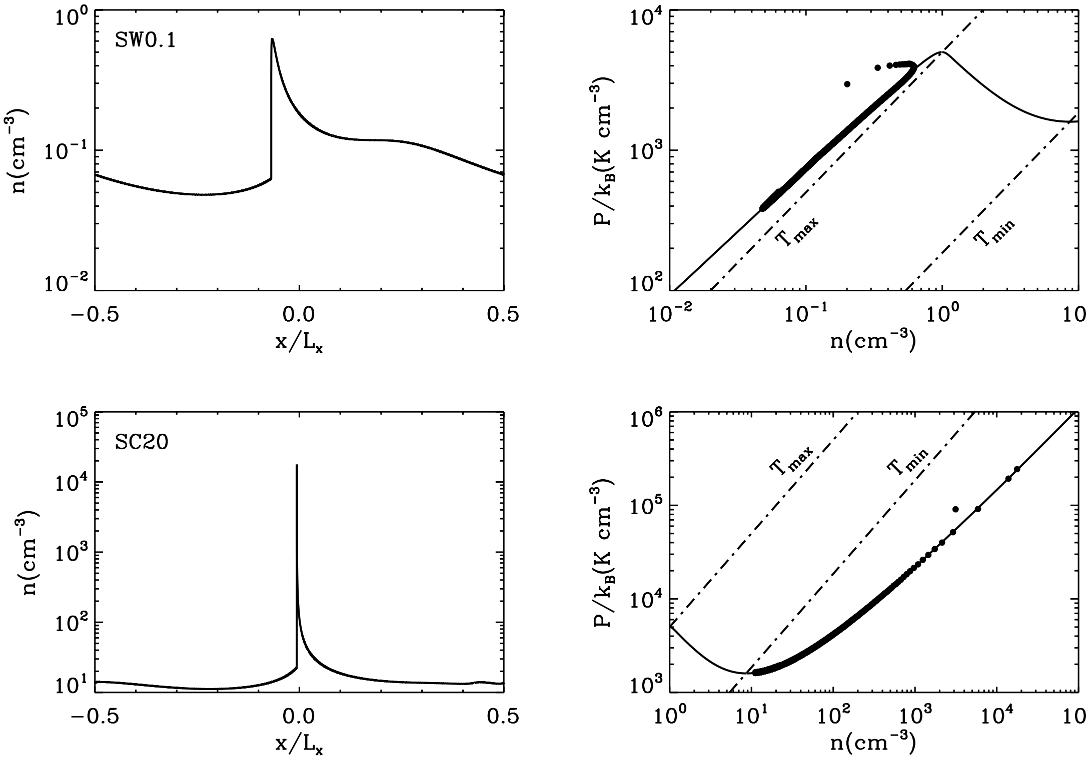

FIG. 8.—Density profiles and scatter plots in the density-pressure plane of models SW0.1 with $n_0 = 0.1$ cm^{-3} (*top*) and SC20 with $n_0 = 20$ cm^{-3} (*bottom*) at $t/t_{\rm cross} = 2.4$. Note that the spiral shocks in these models are smooth and each case contains only a single phase of gas. The shock compression is much stronger for all-cold than all-warm gas because of the higher Mach number.

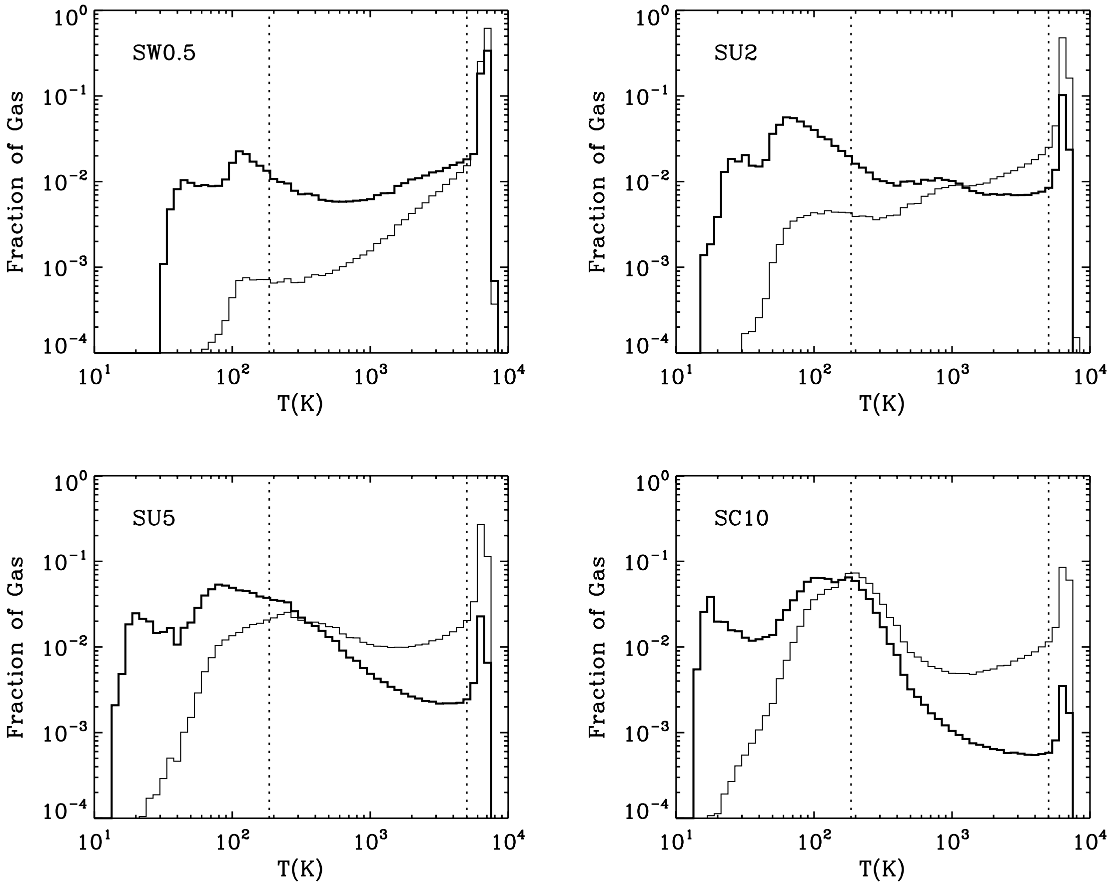

FIG. 9.—Mass-weighted (*thick lines*) and volume-weighted (*thin lines*) temperature PDFs averaged over $t/t_{\rm cross} = 5$–8 for models SW0.1, SU2, SU5, and SC10. In each panel, vertical dotted lines indicate $T_{\rm min}$ and $T_{\rm max}$ to demark the cold, intermediate-temperature, and warm phases. Of the cold component, the gas with $T \lesssim 50$ K is located in the arm region, while cold clouds with $50 \text{ K} \lesssim T \lesssim T_{\rm min}$ are found in the interarm or transition zones.

models with larger n_0. For model SW0.5, on the other hand, introduction of the spiral potential allows only a small fraction of the gas to exceed $P_{\rm min}$ and undergo TI, resulting in a lower cold peak and a higher warm peak than in model SU2. For all the models, the cold peak is fractionally much broader (i.e., larger $\Delta T/T$) than the warm peak.

Of the total intermediate-temperature phase, about 70% is found in the postshock transition zone for models with TI, while the remaining portion resides in boundary layers between the cold and warm phases in the interarm region. Figure 9 shows that the distribution of the intermediate phase is almost flat for model SU2 and increasingly favors lower temperature as n_0 increases. This is because models with larger n_0 have a slower postshock expansion rate and, thus, more gas near $T_{\rm min}$. The mean density and density-weighted mean temperature of the intermediate-temperature gas are found to scale as $n_i \approx 0.41n_0 + 1.29$ and $T_i \approx 4458/(n_0 + 1.81)$ K for $0.5 \lesssim n_0 \lesssim 10$, where n_i and n_0 are in units of cm^{-3}. For the cold and warm phases, the mean values are $n_c \approx 23$ cm^{-3} and $T_c \approx 86$ K and $n_w \approx 0.39$ cm^{-3} and $T_w \approx 6400$ K, respectively, almost independent of n_0. These points lie slightly above $P_{\rm min}$ on the cold and warm branches of the thermal equilibrium curve.

4.4. *Mass and Volume Fractions*

For models with TI, we calculate the mass and volume fractions of three phases averaged over $t/t_{\rm cross} = 5-8$. Figure 10 plots against numerical resolution the mean mass fractions in model SU2, along with the standard deviations as error bars. While the warm mass fraction is fairly insensitive to the number of grid points N, the cold (intermediate-temperature) mass fraction increases (decreases) with increasing resolution for $N \lesssim 10^4$. This is mainly because of the numerical conductivity associated with a large zone size for small N, as explained in § 3. When numerical conductivity is large, the boundary layers in between the cold and warm phases thicken in proportion to the Field length. This increase in the intermediate-temperature mass (in

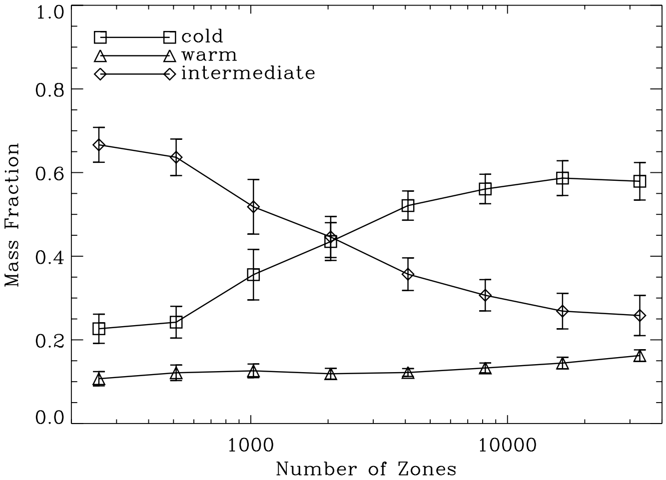

FIG. 10.—Mass fractions of the cold, intermediate-temperature, and warm phases in model SU2 vs. numerical resolution. The numerical results are not affected by numerical conductivity as long as the number of zones is larger than 10^4.

the interarm) occurs primarily at the expense of the cold phase (Begelman & McKee 1990; Ferrara & Shchekinov 1993; Inoue et al. 2006). In addition, large numerical conductivity tends to suppress TI in the postshock transition zone, yielding less cold gas.

Overall, the broadening of interarm cloud interfaces in low-resolution models is responsible for 80% of the increase in the intermediate-temperature mass, while the remaining 20% is due to the suppression of TI in the postshock transition zone. There is no interarm cold gas in models with $N \lesssim 512$, while arm cold gas still exists in these lowest resolution models since the postshock regions are, when fully resolved, denser and broader than interarm clouds and, thus, are less affected by zone averaging. As long as $N \gtrsim 10^4$, the numerical conductivity becomes comparable to, or smaller than, the physical conductivity, and the results are numerically well resolved. Because most of the difference between moderate- and high-resolution models is at warm/cold interfaces, the extremely high resolutions that we find are needed for accurate measurement of the thermally unstable mass fraction would not be required for studies that focus primarily on shock dynamics. We find that the overall shock structures (in terms of the breadth of the transition zone and the time-averaged profiles) are comparable to those in the converged models provided $N \gtrsim 10^3$. At these moderate resolutions, edges of individual clouds are smeared out, but the physically important transition zone downstream from the arm is still recovered.

In the case of model SU2, the converged values of the mass fractions are 59%, 14%, and 27% for the cold, warm, and intermediate-temperature phases, respectively. By volume the cold takes up 4% of the total, while the warm and intermediate-temperature media occupy 70% and 26%, respectively. Since these proportions are 80%, 10%, and 10% by mass and 10%, 80%, and 10% by volume when the spiral potential is weak or absent (e.g., Fig. 3*b*), this implies that spiral shocks and subsequent postshock expansion zone are important for populating the intermediate-temperature portion of the phase plane.

Columns (9)–(14) of Table 1 give the converged values of the mass and volume fractions of each phase in models with multiple phases. Figure 11 plots these proportions as functions of the initial number density n_0. Interestingly, the fraction of mass in the intermediate-temperature phase has a substantial value of $f_i \approx 0.28$, almost independent of n_0.[8] The volume fraction of the intermediate phase increases with $n_0 \lesssim 6$ cm^{-3} and becomes flat at large n_0. Assuming that the cold, warm, and intermediate-temperature phases in each model are represented by the characteristic densities n_c, n_w, and n_i, respectively, mass conservation requires the mass fractions in the cold and warm phases to be $f_c = (1 - n_w/n_0) - (1 - n_w/n_i)f_i$ and $f_w = n_w/n_0 - (n_w/n_i)f_i$, respectively, where $n_c/n_w \gg 1$ is assumed (cf. Piontek & Ostriker 2004). Dotted lines in Figure 11 plot these theoretical f_c and f_w using the empirical results $f_i = 0.28$, $n_w = 0.39$ cm^{-3}, and $n_i = 0.41n_0 + 1.29$ cm^{-3}. These estimates are overall in good agreement with the simulation results.

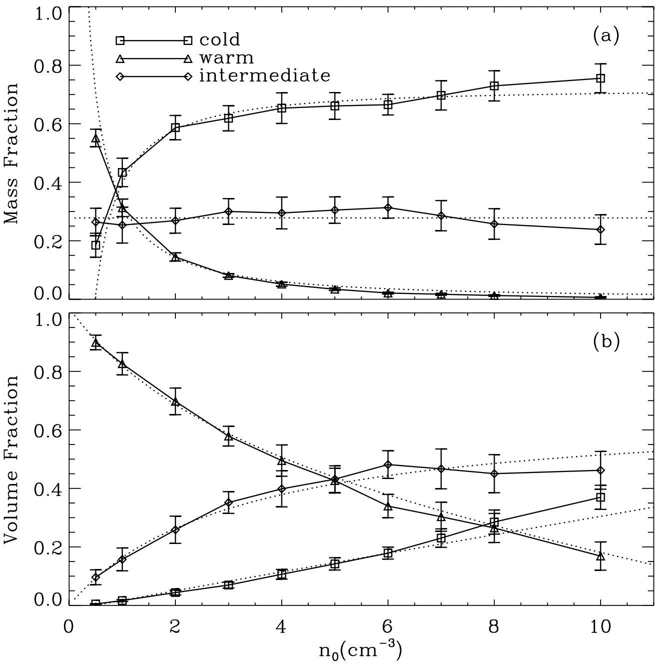

FIG. 11.—Mass and volume fractions of the cold (*squares*), warm (*triangles*), and intermediate-temperature (*diamonds*) phases averaged over $t/t_{\rm cross} = 5-8$, as functions of the initial number density n_0. Error bars indicate the standard deviations of the measurements. Dotted lines show the theoretical estimates computed by adopting a constant value $f_i = 0.28$ for the intermediate-temperature mass fraction.

4.5. *Velocity Dispersions*

Finally, we quantify the level of random gas motions driven in our models due to TI and spiral potential perturbations. Spiral arms produce gas streaming motions that are ordered but vary perpendicular to the shock front. Since streaming velocities are much larger in amplitude than the true random motions, care is needed in measuring the latter. In addition, while the overall shock profiles reach a quasi-steady state after $t/t_{\rm cross} = 5$, several other effects make it difficult to measure turbulent amplitudes in multiphase models: randomly placed cold clouds move with varying speeds in the interarm region, new structures are continuously developing in the transition zone, and the spiral shocks themselves undergo small-amplitude oscillations perpendicular to the shock front. To separate out the background streaming from the total velocity as cleanly as possible, we first construct velocity template profiles $\langle v_x \rangle$ and $\langle v_y \rangle$ for each model, where the angle brackets denote a time average over $t/t_{\rm cross} = 5-8$. Dashed lines in Figures 4*d* and 4*e* show sample $\langle v_x \rangle$ and $\langle v_y \rangle$ profiles in model SU2. We then calculate the density-weighted velocity dispersions using $\sigma_i^2 \equiv \int \rho (v_i - \langle v_i \rangle)^2 dx / (\int \rho\, dx)$ (with $i = x$ or y) in the arm, interarm, and postshock transition zones separately. Figure 12 plots $\sigma_i(t)$ for model SU2, while Figure 13 draws the mean values $\bar{\sigma}_i \equiv \langle \sigma_i^2 \rangle^{1/2}$ along with the standard deviations $\Delta\sigma_i$ for models with multiphase spiral shocks.

Figure 12 shows that the velocity dispersions of the cold phase in the arm region exhibit large-amplitude temporal fluctuations, with characteristic periods of $\sim 0.4 t_{\rm cross}$ and $\sim 0.2 t_{\rm cross}$ for σ_x and σ_y, respectively. These variations of σ_x and σ_y are due to small-amplitude oscillations offsetting the spiral shock front from its mean position. Since streaming varies strongly within the arm (Figs. 4*d* and 4*e*), the offset of the shock position leads to large differences between instantaneous and mean streaming velocities within the arm; these contaminate the measured velocity dispersion at locations near the shock front. During the quasi-periodic oscillations of the spiral shock front, σ_x attains its minimum value when the shock is maximally displaced upstream, while σ_y is smallest when the instantaneous shock front coincides with its mean position. Therefore, the local minima in the time series of σ_x and σ_y correspond to the upper limits to the level of random gas motions inside the arm. For model SU2, the average values

---

[8] By running models with differing F (not listed in Table 1), we found that $f_i \approx 0.040 + 0.045F$[%] for $3\% \leq F \leq 7\%$, but is insensitive to n_0 for the fixed arm parameters.

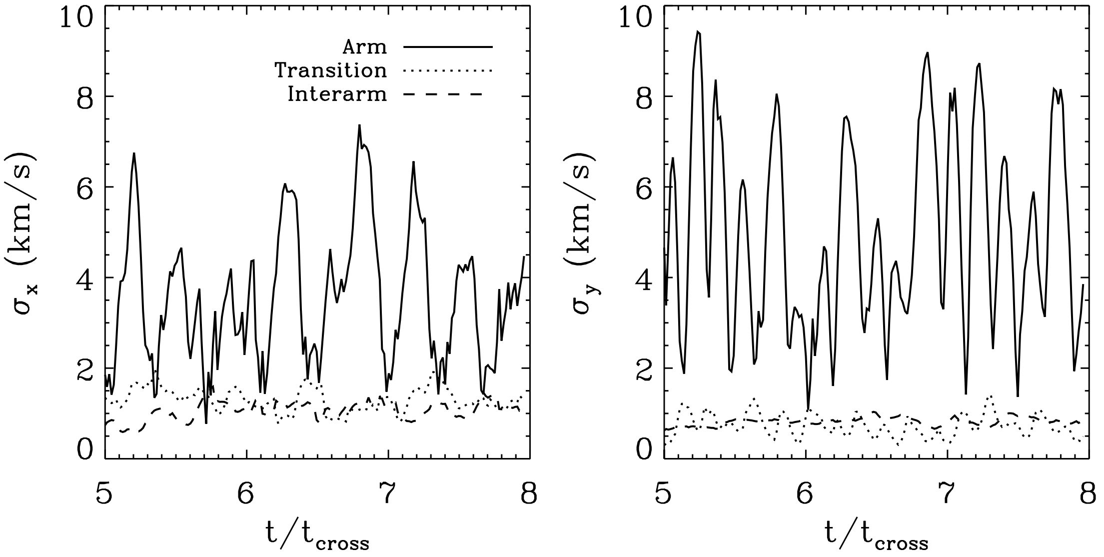

FIG. 12.—Density-weighted velocity dispersions σ_x and σ_y, relative to time-averaged template values, of the gas in the arm (*solid lines*), transition (*dotted lines*), and interarm (*dashed lines*) regions of model SU2. The large-amplitude fluctuations of the velocity dispersions in the arm region are caused by incomplete subtraction of the arm streaming motions. The velocity dispersions in both unstable and interarm regions are not subject to this effect and have mean values of ~1.3 km s^{-1} and ~0.8 km s^{-1} in the *x*- and *y*-directions, respectively.

of the local minima in $\sigma_x(t)$ and $\sigma_y(t)$ are ~2 and ~3 km s^{-1}, respectively, which roughly equals $\bar{\sigma}_i - \Delta\sigma_i$. As Figure 13 shows, $\bar{\sigma}_i - \Delta\sigma_i$ does not vary much with n_0, suggesting that the true velocity dispersion within the arm is relatively independent of mean density.

Unlike their behavior in the arm region, the time-averaged velocity profiles in the interarm and transition zones are relatively smooth, so that the velocity dispersions as calculated in these regions are relatively free of streaming motions. As Figures 12 and 13 show, the velocity dispersions in the interarm and transition zones are similar, amounting to $\bar{\sigma}_x \sim 1.3$ km s^{-1} and $\bar{\sigma}_y \sim 0.8$ km s^{-1} for model SU2 and decreasing slowly with increasing n_0. The ratios of the velocity dispersions in the *x*- to *y*-directions for all regions are consistent with predictions from epicyclic analysis (e.g., Binney & Tremaine 1987), $\bar{\sigma}_y^2/\bar{\sigma}_x^2 = \kappa^2/(4\Omega_0^2) = 1 - q/2$. Here, the local shear rate $q \equiv 2 - (2 - q_0)n/n_0$ is modified from the background value $q_0 \equiv -d \ln \Omega_0/d \ln R$ due to the constraint of potential vorticity conservation (Gammie 1996, 2001; Kim & Ostriker 2001, 2002). For a flat rotation curve ($q_0 = 1$), local shear is reversed inside the arm where the local density exceeds $2n_0$; this in turn increases $\bar{\sigma}_y/\bar{\sigma}_x \approx (n/2n_0)^{1/2}$ above $1/\sqrt{2} = 0.7$. On the other hand, the whole interarm region and most of the unstable region have $n < n_0$, and thus, the ratio $\bar{\sigma}_y/\bar{\sigma}_x$ is smaller than the prediction for a disk without spiral structure.

5. SUMMARY AND DISCUSSION

5.1. *Summary*

Galactic spiral shocks in disk galaxies play an important role in structural and chemical evolution by forming spiral-arm substructures and triggering star formation. Spiral shocks inherently involve large variations in the background density, while cooling

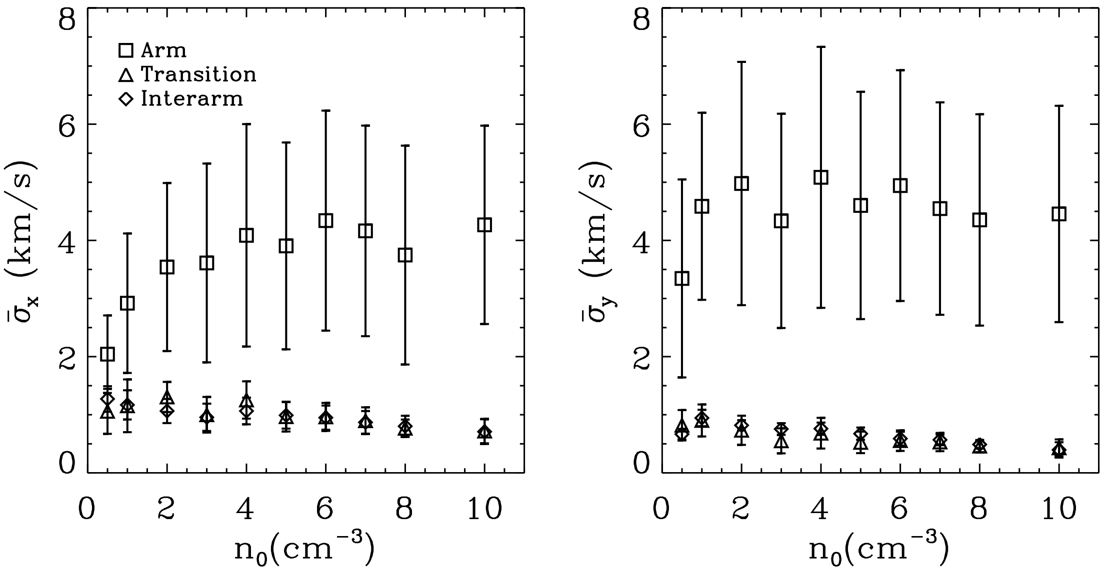

FIG. 13.—Mean values (*symbols*) and standard deviations (*error bars*) of the density-weighted velocity dispersions of each phase during the time span $t/t_{\rm cross} = 5$–8 for models with multiphase spiral shocks.

and heating processes that determine the ISM density and temperature depend rather sensitively on the local state. The interplay between these processes may significantly alter the shock strengths and structures, compared to those computed under an isothermal approximation. In particular, large-scale compressions and expansions across spiral arms may trigger TI, thereby regulating transitions among the different ISM phases. In this paper we have used high-resolution numerical simulations to investigate the dynamics and thermodynamics of this highly nonlinear process. Our models include heating and cooling terms appropriate for atomic gas explicitly in the energy equation and, thus, naturally allow for transitions among cold, warm, and intermediate-temperature phases. The current investigation employs a one-dimensional model in which all the physical quantities vary only in the in-plane direction perpendicular to a local segment of a spiral arm. We allow for gas motions parallel to the arm and include galactic differential rotation. The effects of magnetic fields and self-gravity are neglected in the present paper.

Our main results are summarized as follows.

1. Background flow over the grid, represented by v_{0x} in our models, may result in a significant level of numerical diffusion in finite-difference schemes dealing with the cooling/heating and conduction terms if the numerical resolution is not high enough. We quantify the numerical diffusion of our implementation in terms of an effective numerical conductivity and measure it using growing modes of the TI. By comparing growth rates with predictions from the linear dispersion relation including conduction, we find that the numerical diffusion in the Athena code we use behaves as $\mathcal{K}_n \propto (v_{0x}\Delta x)(\Delta x/\lambda)^p$, where Δx is the grid width, p is the order of spatial reconstruction method ($p = 2$ for PLM and 3 for PPM), and λ is the spatial wavelength. For typical values of $v_{0x} = 13$ km s^{-1}, $\Delta x = 0.04$ pc, and $\lambda = 3.5$ pc in our models, the numerical conductivity with the PLM amounts to $\mathcal{K}_n \sim 2.3 \times 10^5$ erg s^{-1} cm^{-1} K^{-1}, comparable to the physical conductivity $\mathcal{K}_0 = 10^5$ erg s^{-1} cm^{-1} K^{-1} adopted in the current work.

2. Stellar spiral potential perturbations induce shocks that reach a quasi-steady state after a few orbits. The resulting flow contains phase transitions provided the mean gas density is in the range 0.5 cm^{-3} $\leq n_0 \leq$ 10 cm^{-3}, for the parameters considered in the present work. Models with $n_0 \leq 0.1$ cm^{-3} or $n_0 \geq 20$ cm^{-3} yield single-phase spiral shock profiles. We divide the flow into three distinct zones based on thermal regime: arm, interarm, and transition. The "arm" refers to the highly compressed postshock region filled with cold gas at $T < T_{\rm min} = 185$ K, while in the "interarm" region far from the shock most of the volume is occupied by warm gas with $T > T_{\rm max} = 5012$ K. The "transition" zone corresponds to the expanding region downstream from the arm where intermediate-temperature gas ($T_{\rm min} < T < T_{\rm max}$) undergoes TI. Figure 5 summarizes the evolutionary cycle in the density-pressure plane: the warm/cold interarm gas (A_1/A_2) is shocked (B_1/B_2) and immediately cools to become the denser cold arm gas (C_1/C_2); this subsequently enters the unstable transition zone (D) and evolves back into the warm and cold interarm phases. For our standard model SU2 with mean density $n_0 = 2$ cm^{-3}, the duration of the arm, transition, and interarm stages are approximately 14%, 22%, and 64% of the cycle, respectively, occupying roughly 1%, 16%, and 83% of the simulation domain.

3. At late times, instantaneous profiles in models with TI show many density spikes representing cold clouds. Time-averaged profiles are, however, relatively smooth, and the density peaks representing the arm are more symmetric than in nondiffusive, isothermal models. We find that a viscous isothermal model with $T = 1000$ K and a mean free path of $l_0 = 100$ pc yields a similar peak density and arm width to the average profile from model SU2. This confirms the notion that for purposes where detailed ISM knowledge is not needed, multiphase effects on shocks can be approximately treated via viscosity modeling excursions and collisions of dense clouds, as suggested by Cowie (1980) and Lubow et al. (1986). Simulations such as those we have performed are needed in order to calibrate the viscous/isothermal model parameters, however.

4. For models with multiphase spiral shocks, intermediate-temperature gas amounts to ~0.25–0.3 of the total by mass, insensitive to n_0. Of this, about 70% is found in the transition zone, while the remaining 30% lies at interfaces between the cold and warm media. This suggests that the postshock expanding flows, an inherent feature of galactic spiral structure, are important for producing intermediate-temperature gas. The mean density and density-weighted mean temperature of the intermediate-temperature phase are found to be $n_i = 0.41n_0 + 1.29$ cm^{-3} and $T_i = 4458/[(n_0/1\ {\rm cm}^{-3}) + 1.81]$ K, respectively. The fractions of the cold and warm phases are 59% and 14% by mass and 4% and 70% by volume for model SU2, respectively, and vary with n_0 according to simple expectations based on mass conservation with a prescribed density in each phase.

5. We find that one-dimensional spiral shocks with multiphase gas produce nonnegligible random gas motions. At late times, the gas in both interarm and transition zones has typical density-weighted velocity dispersions of $\sigma_x \sim 1.3$ km s^{-1} and $\sigma_y \sim 0.8$ km s^{-1} in the directions perpendicular and parallel to the spiral arms, respectively. This is transonic with respect to the cold medium and subsonic with respect to the warm medium. The cold gas in the arms is estimated to have slightly larger values $\sigma_x \sim 2$ km s^{-1} and $\sigma_y \sim 3$ km s^{-1}, although true turbulence levels may be slightly lower, because it is difficult to fully subtract streaming motions in the arm region.

5.2. *Discussion*

Since the growth rates of pure TI are maximized at the smallest available wavelengths, growth of grid scale noise dominates numerical simulations if it is not suppressed. To prevent this numerical problem, it is customary to include thermal conduction that preferentially stabilizes small-scale perturbations (e.g., Piontek & Ostriker 2004, 2005) and also broadens the transition layer between cold and warm phases (e.g., Begelman & McKee 1990). Koyama & Inutsuka (2004) studied TI in an initially static medium and showed that numerical results converge only if these conductive interfaces are well resolved. They found that this requires the cell size to be less than one-third of the Field length. In modeling systems with large turbulent (e.g., Gazol et al. 2005) or ordered (this work) velocity flows over the grid, numerical conductivity may be considerable if resolution is inadequate. The convergence study presented in § 4.4 suggests that the convergence criterion of Koyama & Inutsuka (2004) is valid in a moving medium, too, with the condition that the grid spacing must be smaller than the *effective* Field length based on the total (physical + numerical) conductivity.

In earlier work, Tubbs (1980) and Marochnik et al. (1983) performed time-dependent simulations of galactic spiral shocks that included cooling and heating, but their models appear to suffer from large numerical conductivity associated with insufficient resolution. While they showed that phase transitions from warm gas to cold clouds do occur in some models at the shock locations, they were unable to resolve the postshock transition zone.

In particular, the $n_0 = 0.5$ cm^{-3} model shown in Figure 7 of Marochnik et al. (1983) exhibits a smooth density profile without any indication of TI although much of the region is occupied by gas with densities and temperatures in the unstable range.[9] This is presumably because large numerical conductivity (due to low resolution) renders the time and/or length scales of TI in their simulations longer than the duration and/or width of the postshock transition zone. Indeed, we find that when we run our own models at low resolution (e.g., with 512 zones or less for model SC10), the numerical conductivity is large enough that the gas in the transition zone does not undergo TI and instead smoothly converts to the interarm warm phase.

In terms of their time-averaged properties, the overall dynamics and flow characteristics of spiral shocks with TI remain similar to those of isothermal spiral shocks (e.g., Roberts 1969; Shu et al. 1973; Woodward 1975; Kim & Ostriker 2002). The salient features of spiral shocks with thermal evolution include the facts that they allow phase transitions at the shock front (from warm to cold) and in the postshock transition zone (from cold to warm) and that there are cold clumps in the interarm region. Given the very high density and pressure within the arm, cold gas downstream from the shock front would transform to molecular clouds if self-gravity and chemical reactions for molecule formation were included. By running smoothed particle hydrodynamics simulations with separate cold and warm "particles," Dobbs & Bonnell (2007) indeed found that the density of the cold component inside arms is sufficient to form molecules (see also Dobbs & Price 2008). These authors did not allow for phase transitions between the cold and warm components, however, which is an essential aspect of the evolution (cf. Shu et al. 1972).

A postshock transition zone, where the gas is predominantly in the intermediate-temperature range, is a necessary feature of any quasi-steady state. About 40% of the atomic gas in the local Milky Way is observed to be the cold neutral medium (Heiles 2001; Heiles & Troland 2003), which is consistent with our results for mean density $n_0 = 1$ cm^{-3}, similar to the local Milky Way value.[10] Heiles & Troland (2003) also find that about half of the remaining atomic gas is consistent with being thermally stable warm neutral medium, while the balance is in the unstable temperature range 500–5000 K. These fractions are also comparable to what we find for $n_0 = 1$ cm^{-3}. The presence of thermally unstable gas has been interpreted as owing to dynamical effects which act on timescales comparable to the heating and cooling times. Dynamical processes that have been investigated include magnetorotational instability (Piontek & Ostriker 2004, 2005, 2007), colliding flows (Audit & Hennebelle 2005; Heitsch et al. 2005, 2006; Vázquez-Semadeni et al. 2006), energy injection from OB stars (Vázquez-Semadeni et al. 2000; Gazol et al. 2001), and supernova explosions (Avillez & Breitschwerdt 2005; Mac Low et al. 2005). Here, we have shown that even without these additional small-scale energy sources, a significant amount of intermediate-temperature gas forms as a natural product of large-scale spiral shocks with TI, primarily in the expanding region downstream from the arm.

Many numerical studies of TI have shown that turbulent amplitudes driven by "pure TI" *alone* are quite small. For example, Piontek & Ostriker (2004) showed that pure TI in an initially static, uniform medium in thermal equilibrium produces only a modest level of random gas motions, $\sigma \sim 0.2-0.3$ km s^{-1}. Kritsuk & Norman (2002a, 2002b) similarly found that TI of gas starting from thermal equilibrium, or with time-dependent heating, results in only subsonic turbulence, $\sigma \sim 0.2$ km s^{-1} when the cold gas dominates. The velocity dispersions $\sigma \sim 1.5$ km s^{-1} of the gas found in the interarm and transition zones in our one-dimensional models are significantly larger than those from pure TI. These velocities are much lower than those we found in previous (isothermal) simulations (Kim & Ostriker 2006; Kim et al. 2006) in which the vertical shock structure is resolved, however. Evidently, shock flapping offers a more effective means of converting galactic rotation to turbulence than simple in-plane oscillations. Work is currently underway to see how TI interacts with vertically resolved spiral shocks—and differential buoyancy of cold and warm gas—to generate turbulence and structure in the ISM.

We thank A. Kritsuk for drawing our attention to earlier work of Marochnik et al. on spiral shocks with thermal instability. This work was supported by the Korea Research Foundation Grant funded by the Koran Government (MOEHRD; KRF-2007-313-C00328). The work of E. C. O. on this project was supported by the US National Science Foundation under grant AST 05-07315. The numerical computations presented in this work were performed on the Linux cluster at KASI (Korea Astronomy and Space Science Institute) built with funding from KASI and ARCSEC.

---

[9] The heating and cooling functions adopted by Marochnik et al. (1983) have the critical densities demarcating the warm, intermediate-temperature, and cold phases about 20 times smaller than those in the present work. Thus, their model with $n_0 = 0.5$ cm^{-3} corresponds to our model SC10, which develops multiphase structure.

[10] The value of n_0 that produces the numerical results consistent with observations may differ in models with different L_x, since the fractional size of the transition region is likely to depend on the ratio of cooling time to arm-to-arm crossing time.

REFERENCES

Audit, E., & Hennebelle, P. 2005, A&A, 433, 1
Baade, W. 1963, in The Evolution of Stars and Galaxies, ed. C. Payne-Gaposchkin (Cambridge: Harvard Univ. Press), 218
Baker, P. L., & Barker, P. K. 1974, A&A, 36, 179
Balbus, S. A. 1988, ApJ, 324, 60
Balbus, S. A., & Cowie, L. L. 1985, ApJ, 297, 61
Begelman, M. C., & McKee, C. F. 1990, ApJ, 358, 375
Binney, J., & Tremaine, S. 1987, Galactic Dynamics (Princeton: Princeton Univ. Press)
Boley, A. C., & Durisen, R. H. 2006, ApJ, 641, 534
Cowie, L. L. 1980, ApJ, 236, 868
Cox, D. P., & Smith, B. W. 1974, ApJ, 189, L105
de Avillez, M. A., & Breitschwerdt, D. 2004, A&A, 425, 899
———. 2005, A&A, 436, 585
Dobbs, C. L., & Bonnell, I. A. 2006, MNRAS, 367, 873
———. 2007, MNRAS, 376, 1747
Dobbs, C. L., & Price, D. J. 2008, MNRAS, 383, 497
Elmegreen, B. G. 1994, ApJ, 433, 39
Elmegreen, B. G., & Elmegreen, D. M. 1983, MNRAS, 203, 31
———. 1986, ApJ, 311, 554
Elmegreen, D. M. 1980, ApJ, 242, 528
Elmegreen, D. M., Elmegreen, B. G., Kaufman, M., Sheth, K., Struck, C., Thomasson, M., & Brinks, E. 2006, ApJ, 642, 158
Ferrara, A., & Shchekinov, Y. 1993, ApJ, 417, 595
Ferriere, K. 1998, ApJ, 503, 700
———. 2001, Rev. Mod. Phys., 73, 1031
Field, G. B. 1965, ApJ, 142, 531
Field, G. B., Goldsmith, D. W., & Habing, H. J. 1969, ApJ, 155, L149
Fujimoto, M. 1968, in IAU Symp. 29, Non-stable Phenomena in Galaxies, ed. A. Arakelyan (Yerevan: Armenian Acad. Sci.), 453
Gammie, C. F. 1996, ApJ, 462, 725
———. 2001, ApJ, 553, 174
Gardiner, T. A., & Stone, J. M. 2005, J. Comput. Phys., 205, 509
Gazol, A., Vázquez-Semadeni, E., & Kim, J. 2005, ApJ, 630, 911

Gazol, A., Vázquez-Semadeni, E., Sánchez-Salcedo, F. J., & Scalo, J. 2001, ApJ, 557, L121
Gerola, H., & Seiden, P. E. 1978, ApJ, 223, 129
Gómez, G. C., & Cox, D. P. 2002, ApJ, 580, 235
———. 2004, ApJ, 615, 744
Gordon, K. 2007, Spitzer Press Release (Pasadena: Caltech), http://gallery.spitzer.caltech.edu/Imagegallery/image.php?imagename=sig07-025
Hawley, J. F., Gammie, C. F., & Balbus, S. A. 1995, ApJ, 440, 742
Heiles, C. 2001, ApJ, 551, L105
Heiles, C., & Troland, T. H. 2003, ApJ, 586, 1067
Heitsch, F., Burkert, A., Hartmann, L. W., Slyz, A. D., & Devriendt, J. E. G. 2005, ApJ, 633, L113
Heitsch, F., Slyz, A. D., Devriendt, J. E. G., Hartmann, L. W., & Burkert, A. 2006, ApJ, 648, 1052
Inoue, T., Inutsuka, S., & Koyama, H. 2006, ApJ, 652, 1331
Jenkins, E. B., & Tripp, T. M. 2007, in IAU Symp. 237, Triggered Star Formation in a Turbulent ISM, ed. B. G. Elmegreen & J. Palous (Cambridge: Cambridge Univ. Press), 53
Kennicutt, R. C. 2004, Spitzer Press Release (Pasadena: Caltech), http://www.spitzer.caltech.edu/Media/releases/ssc2004-19/ssc2004-19a.shtml
Kim, C.-G., Kim, W.-T., & Ostriker, E. C. 2006, ApJ, 649, L13
Kim, W.-T., & Ostriker, E. C. 2001, ApJ, 559, 70
———. 2002, ApJ, 570, 132
———. 2006, ApJ, 646, 213
Knapen, J. H., Cepa, J., Beckman, J. E., Soledad del Rio, M., & Pedlar, A. 1993, ApJ, 416, 563
Koyama, H., & Inutsuka, S. 2002, ApJ, 564, L97
———. 2004, ApJ, 602, L25
Kritsuk, A. G., & Norman, M. L. 2002a, ApJ, 569, L127
———. 2002b, ApJ, 580, L51
La Vigne, M. A., Vogel, S. N., & Ostriker, E. C. 2006, ApJ, 650, 818
Lubow, S. H., Balbus, S. A., & Cowie, L. L. 1986, ApJ, 309, 496
Lynden-Bell, D. 1966, Observatory, 86, 57
Mac Low, M.-M., Balsara, D. S., Kim, J., & Avillez, M. A. 2005, ApJ, 626, 864
Marochnik, L. S., Berman, B. G., Mishurov, Yu. N., & Suchkov, A. A. 1983, Ap&SS, 89, 177
Martos, M. A., & Cox, D. P. 1998, ApJ, 509, 703
McKee, C. F., & Ostriker, J. P. 1977, ApJ, 218, 148
Meerson, B. 1996, Rev. Mod. Phys., 68, 215
Mufson, S. L. 1974, ApJ, 193, 561
Parker, E. N. 1953, ApJ, 117, 431
Piontek, R. A., & Ostriker, E. C. 2004, ApJ, 601, 905
———. 2005, ApJ, 629, 849
———. 2007, ApJ, 663, 183
Rand, R. J., & Kulkarni, S. R. 1990, ApJ, 349, L43
Roberts, W. W. 1969, ApJ, 158, 123
Roberts, W. W., & Yuan, C. 1970, ApJ, 161, 887
Scoville, N. Z., Polletta, M., Ewald, S., Stolovy, S. R., Thompson, R., & Rieke, M. 2001, AJ, 122, 3017
Scoville, N., & Rector, T. 2001, HST Press Release (Baltimore: STScI), http://oposite.stsci.edu/pubinfo/PR/2001/10/index.html
Seigar, M. S., & James, P. A. 2002, MNRAS, 337, 1113
Shetty, R., & Ostriker, E. C. 2006, ApJ, 647, 997
Shetty, R., Vogel, S. N., & Ostriker, E. C., & Teuben, P. T. 2007, ApJ, 665, 1138
Shu, F. H., Milione, V., Gebel, W., Yuan, C., Goldsmith, D. W., & Roberts, W. W. 1972, ApJ, 173, 557
Shu, F. H., Milione, V., & Roberts, W. W. 1973, ApJ, 183, 819
Sleath, J. P., & Alexander, P. 1996, MNRAS, 283, 358
Tubbs, A. D. 1980, ApJ, 239, 882
Vázquez-Semadeni, E., Gazol, A., & Scalo, J. 2000, ApJ, 540, 271
Vázquez-Semadeni, Gómez, G. C., Jappsen, A.-K., Ballesteros-Paredes, J., González, R. F., & Klessen, R. S. 2007, ApJ, 657, 870
Vázquez-Semadeni, E., Ryu, D., Passot, T., González, R. F., & Gazol, A. 2006, ApJ, 643, 245
Vogel, S. N., Kulkarni, S. R., & Scoville, N. Z. 1988, Nature, 334, 402
Wada, K., & Koda, J. 2004, MNRAS, 349, 270
Willner, S. P., et al. 2004, ApJS, 154, 222
Wolfire, M. G., McKee, C. F., Hollenbach, D., & Tielens, A. G. G. M. 2003, ApJ, 587, 278
Woodward, P. R. 1975, ApJ, 195, 61
———. 1976, ApJ, 207, 484